

Nonlinear co-generation of graphene plasmons for optoelectronic logic gates

Yiwei Li

University of Electronic Science and Technology of China

Ning An

University of Electronic Science and Technology of China

Zheyi Lv

Hunan University

Yucheng Wang

University of Electronic Science and Technology of China

Bing Chang

University of Electronic Science and Technology of China

Teng Tan

University of Electronic Science and Technology of China <https://orcid.org/0000-0003-1820-3618>

Xuhan Guo

Shanghai Jiao Tong University

Xizhen Xu

Shenzhen University

Jun He

Shenzhen University

Handing Xia

China Academic of Engineering Physics

Zhaohui Wu

China Academic of Engineering Physics

Yikai Su

Shanghai Jiao Tong University

Yuan Liu

Hunan University <https://orcid.org/0000-0002-0024-9290>

Yun-Jiang Rao

University of Electronic Science and Technology of China <https://orcid.org/0000-0003-0717-5586>

Giancarlo Soavi

Friedrich Schiller University Jena <https://orcid.org/0000-0003-2434-2251>

BAICHENG YAO (✉ yaobaicheng@uestc.edu.cn)

University of Electronic Science and Technology of China <https://orcid.org/0000-0001-8368-5815>

Letter

Keywords:

Posted Date: January 12th, 2022

DOI: <https://doi.org/10.21203/rs.3.rs-1204181/v1>

License:  This work is licensed under a Creative Commons Attribution 4.0 International License.

[Read Full License](#)

Version of Record: A version of this preprint was published at Nature Communications on June 6th, 2022. See the published version at <https://doi.org/10.1038/s41467-022-30901-8>.

Abstract

Surface plasmons in graphene provide a compelling strategy for advanced photonic technologies thanks to their tight confinement, fast response and tunability. Recent advances in the field of all-optical generation of graphene's plasmons in planar waveguides offer a promising method for high-speed signal processing in nanoscale integrated optoelectronic devices. Here, we use two counter propagating frequency combs with temporally synchronized pulses to demonstrate deterministic all-optical generation and electrical control of multiple plasmon polaritons, excited via difference frequency generation (DFG). Electrical tuning of a hybrid graphene-fiber device offers a precise control over the DFG phase-matching, leading to tunable responses of the graphene's plasmons at different frequencies and provides a powerful tool for high-speed logic operations. Our results offer new insights for plasmonics on hybrid photonic devices based on layered materials and pave the way to high-speed integrated optoelectronic computing circuits.

Introduction

Nano-photonic technologies hold great promises for and high-speed signal processing, as they circumvent light-electron conversion and offer the ideal solution to the problems of heat generation and limited bandwidth that are typical of electronic circuits [1, 2]. In recent years, intense research in the field of optical computing has led to novel and advanced solutions for high-speed modulation and demodulation [3, 4, 5], metamaterial analog processing [6, 7], optoelectronic convolution [8, 9], machine learning [10, 11, 12, 13] and quantum computing [14]. Since logic gates are the most fundamental building-block of classical and quantum computing [15], their development is nowadays of paramount importance. While classical electrical computing is based on transistors, a gold standard for optical logic gates is still elusive. For instance, by exploiting the linear interference in micro-rings and micro-couplers, optical logic operations have been successfully obtained on chip [16, 17, 18, 19, 20]. However, the diffraction limit [21] hinders further miniaturization of such devices and creates a bottleneck for industrial expansion.

On the other hand, due to their high resonant frequencies (\approx tens of THz) and unique field confinement (\approx hundreds of nm) [22, 23], graphene plasmons are promising candidates for the realization of miniaturized photonic integrated signal-processing elements beyond the diffraction limit of light [24, 25]. In addition, in contrast to noble metals, graphene's plasmons display flexible electrical tunability [26, 27, 28], which in turn offers a powerful knob for dynamic information processing. Thanks to the strong nonlinear response of graphene [29, 30, 31, 32], such electrically tunable plasmons can be generated all-optically and subsequently manipulated and detected directly on-chip [33, 34], providing a viable strategy for planar integration in high-density optoelectronics. The main downside of the conventional methods that are used for nonlinear generation of plasmons in graphene is the necessity of a careful laser scanning, which is typically slow and has limited bandwidth and thus prevents the realization of ultrafast logic operations.

Here, we exploit difference-frequency-generation (DFG) to demonstrate multiple plasmons co-generation in a hybrid graphene photonic device. In this scheme, two synchronized and stabilized mode-locked lasers (*i.e.*, laser frequency combs) [35, 36] are counter propagating inside a hybrid graphene/D-shaped fiber and are used as pump and probe pulses for the DFG in a broad frequency range up to 50 THz. In particular, we simultaneously detect multiple plasmon peaks thanks to the broadband frequency-momentum conservation. Finally, by electrically tuning the graphene's Fermi level we show individual modulation of each of the co-generated plasmons. This provides a powerful method to realize different logic operations (AND, OR, NOR) on a single integrated photonic device.

Results

Figure 1a shows a sketch of the graphene/D-shaped fiber (GDF) used in this work. A section of a silica single mode fiber was side-polished, and a monolayer graphene was deposited on top of the planar surface (see Methods for details). Two gold electrodes (channel width $\approx 200 \mu\text{m}$) are used for the electrical tuning of the graphene's Fermi level [37]. The fiber core is $6 \mu\text{m}$ in diameter and light-graphene interaction occurs via evanescent waves [38]; the total linear losses of the graphene-fiber heterostructure are $< 0.5 \text{ dB}$. Further details on the nanofabrication of the GDF are provided in Supplementary Section S2. In the DFG process used for plasmon generation, graphene acts both as the second-order nonlinear medium and as the nanoscale plasmon waveguide. Driven by the out-of-plane second-order nonlinear susceptibility $\chi^{(2)}$ of the GDF, the high frequency pump photon (f_{pump}) splits into a (counter propagating) lower frequency probe photon (f_{probe} counter-propagating) and a plasmon (f_{sp} , co-propagating). The DFG requires both energy conservation $f_{sp} + f_{probe} = f_{pump}$ and momentum conservation $k_{pump} = k_{sp} + k_{probe}$ where $\hbar k_{sp}$, $\hbar k_{probe}$ and $\hbar k_{pump}$ are the momenta of the plasmon, probe and pump respectively. Considering the scalar dispersion relation $k = 2\pi f n / c$, the momentum conservation can be re-written as $f_{sp} n_{sp} = f_{pump} n_{pump} + f_{probe} n_{probe}$. In order to generate plasmons in graphene via the DFG process, all the optical modes must have transverse magnetic (TM) polarization that probes the non-centrosymmetric out-of-plane direction of the hybrid device, while graphene is centrosymmetric for in-plane excitation [39, 40]. As an example, Fig. 1b simulates the side-view electric field distributions of the pump and the plasmon modes when $f_{pump} = 192 \text{ THz}$ and $f_{sp} = 10 \text{ THz}$.

Figure 1c shows a top-view optical image of the GDF. The fiber core is denoted by a white dashed line and graphene is deposited on the fiber and connected *via* the source and drain electrodes (Au). Unlike typical back-gate field-effect-transistors [41], this on-fiber Au-graphene-Au transistor is driven by current rather than gate voltage [42]. Within the Drude's model, the surface plasmon frequency f_{sp} is defined by the graphene's dispersion relation which, in turn, depends on the Fermi level: a higher carrier density induces a higher f_{sp} . In our GDF architecture, by changing the source-drain voltage (V_D) in the range 0 to 1 V, we can tune the effective graphene Fermi level $|E_F|$ from ≈ 0 to 0.4 eV. Fig. 1d (top panel) plots the measured device resistance and the calculated $|E_F|$ as a function of V_D . When $V_D = 0 \text{ V}$ graphene is intrinsically positively charged (p-doped) with $|E_F| \approx 0.1 \text{ eV}$. By increasing V_D we drive a current in the graphene

channel and shift E_F towards the Dirac point and the upper Dirac cone (n-doping). The graphene's resistance reaches the maximum (Dirac point) when $V_D = 0.16$ V. To confirm the V_D dependence of E_F , we have also characterized the doping via in-situ Raman spectroscopy (see Supplementary Section S3).

The bottom panel of Fig. 1d plots the two frequency combs that are used for the DFG experiments. Comb 1 (blue curve, pump) is a stabilized Er mode-locked laser with tunable central wavelength ≈ 1560 nm, 3-dB bandwidth ≈ 7.5 THz, and maximum average power of ≈ 30 mW. Meanwhile, Comb 2 (red curve, probe) is spectrally flat in the wavelength region ≈ 1500 nm - 2100 nm and it is obtained by supercontinuum generation starting from Comb 1 (see Methods for details). The two combs are locked with the same repetition rate of ≈ 38 MHz and their temporal overlap can be controlled experimentally by a delay line. In the DFG experiments, the two combs are launched into the GDF from opposite directions (the experimental setup is shown in Supplementary Section S3). We further note that in order to achieve co-generation of multiple plasmons and detect them accurately, the pump should be spectrally sharp while the probe must be broadband and spectrally flat. The following scenario can now occur: for those frequencies that satisfy the phase-matching condition, the simultaneous presence (time-overlap) of the pump (*Comb 1*) and the probe (*Comb 2*) will lead to the generation of a plasmon and to the enhancement of the counter-propagating probe (*Comb 2*). Thus, the plasmon generation and the DFG process can be detected as an increase of the probe intensity at a specific phase-matched frequency (ΔI_{DFG}), in analogy with the widely used process of optical parametric amplification [43].

For example, for a pump wavelength of 1560 nm (192.308 THz) and a nonlinearly excited plasmon at $f_{sp} = 10$ THz, we will observe a peak on the flat spectrum of *Comb 2* (probe enhancement) at ≈ 1645.57 nm (182.308 THz). To further prove that this peak arises from DFG, we modulated the pump at 500 kHz and observed the same modulation in the counter-propagating probe comb (see Supplementary Section S3). In contrast to conventional schemes that use continuous-wave tunable lasers for plasmon generation [33], our two-combs approach doesn't require time to scan the laser wavelengths and operates with ≈ 2 orders of magnitude less average optical power. More importantly, due to the large bandwidth (50 THz) of the probe comb, this scheme enables us to find high frequency plasmons beyond the limitation of any near-infrared tunable lasers.

Figure 1e shows the parametric space of the DFG process. To generate the THz graphene plasmons, the phase-matching condition for the counter-pumped DFG and the dispersion of the plasmonic modes must match. For free-standing graphene, the plasmonic dispersion is defined by the Drude's model ($k_{sp} \propto f_{sp}^2$) [25]: The blue curves in Figure 1e are exemplary cases when $|E_F| = 0.1$ eV and 0.4 eV. On the other hand, the phase-matching condition for DFG can be re-written as $(c/2\pi)k_{sp} = -f_{sp}n_{probe} + f_{pump}(n_{pump} + n_{probe})$. When tuning the pump comb from lower to higher frequency (e.g., from 1530 nm to 1610 nm as shown in Figure 1e), the red curve moves from right to left. Since graphene plasmons are generated only at the intersections of the graphene dispersion curves and the DFG phase-matching lines, by tuning the graphene's Fermi level and the pump frequency, the plasmons' frequency will shift within the yellow region of Figure 1e.

Figure 2 shows the electrical tunability of our device. In the measurements, we have a central $f_{pump} = 192.3$ THz (1560 nm) while the probe pulse is broadband. Fig. 2a, 2b and 2c show the graphene's plasmon dispersion calculated using the random phase approximation (RPA) [23] at $|E_F| = 0.1$ eV, 0.2 eV and 0.3 eV respectively. Here, we considered two surface-optical phonon resonances [44, 45] of the silica substrate (fiber), located at $f_1 = 24$ THz and $f_2 = 35$ THz (white solid lines). The phase matching condition for the DFG is marked by the white dashed line and we used for the refractive inside the fiber's core $n_{pump} \approx n_{probe} = 1.45$. When $|E_F| = 0.1$ eV (Fig. 2a) the graphene's plasmon is far below the silicon phonon frequency, hence we can only see one DFG peak at 1623 nm ($f_{sp} = 7.5$ THz). When $|E_F| = 0.2$ eV (Fig. 2b) the graphene's plasmon interacts with the 24 THz phonon resonance, dividing the Drude curve into two branches. In this case, we observe two DFG peaks located at 1655 nm and 1804 nm ($f_{sp} = 11$ THz and 26 THz). Finally, when $|E_F| = 0.3$ eV (Fig. 2c) hybridization of the graphene's plasmon with the substrate phonons leads to three branches and we observe enhanced DFG peaks at 1672 nm, 1813 nm and 1923 nm ($f_{sp} = 13$ THz, 27 THz and 36 THz). In addition, based on the dispersion relation $n_{sp} = (f_{pump}n_{pump} + f_{probe}n_{probe})/(f_{pump} - f_{probe})$, we can estimate the effective refractive index of the plasmonic modes. For instance, when $f_{sp} \approx 7.5, 27$ THz and 36 THz we obtain $n_{sp} \approx 68, 19$ and 14, suggesting strong confinement of the plasmons. The simulated fiber mode indices are shown in Supplementary Section S1.

In order to further confirm the nature of the observed signal and distinguish it from other possible side effects (*e.g.*, saturable absorption), in Fig. 2c and 2d we analyze the conversion efficiency of ΔI_{DFG} . In particular, the generation of plasmons and the consequent intensity enhancement at f_{probe} relies on the consumption of the pump. We thus fix the probe power to 10 mW while increasing the pump power, and we measure both the pump transmission and the total ΔI_{DFG} at different values of $|E_F|$. For low pump power values (< 8 mW), the curves at $|E_F| = 0.1$ eV and 0.2 eV are almost identical, while the curve at $|E_F| = 0.3$ eV shows higher transmission, likely due to reduced absorption in the thermally broadened Fermi Dirac distribution (considering the pump photon energy of ≈ 0.8 eV). Initially, the transmission curves for all $|E_F|$ values increase with pump power and reach a plateau at ≈ 12 mW due to saturable absorption [46]. Subsequently, for pump powers > 12 mW, graphene is fully saturated and a further increase of the power leads to a lower transmission due to pump consumption *via* the DFG process. For the same value of the pump power (> 12 mW) we observe that the ΔI_{DFG} raises from the noise floor and subsequently increases linearly (Fig. 2d), as expected for DFG considering $I_{sp} = \Delta I_{DFG}(f_{sp}/f_{probe}) = [\chi^{(2)}]^2 I_{pump} I_{probe} / L_{sp}^2$, where L_{sp} is the transmission loss of the plasmon. From a linear fit of the DFG conversion efficiency in Fig. 2d, we obtain a $[\chi^{(2)}]^2 / L_{sp}^2$ at $|E_F| = 0.3$ eV of $\approx 10^{-4} \text{ W}^{-1}$, in agreement with theoretical values [30].

In Fig. 3 we show the ultrafast nature of our method by scanning the delay between the pump and probe combs while measuring the DFG enhanced signal (ΔI_{DFG}), in analogy with an auto-correlation measurement (Fig. 3a, see also the implementation in Supplementary Video S1). Fig. 3b, 3c and 3d show the time-dependent DFG for $V_D = 0$ V ($|E_F| = 0.1$ eV), $V_D = 0.4$ V ($|E_F| = 0.2$ eV), and $V_D = 0.6$ V ($|E_F| = 0.3$ eV) respectively. At zero delay time we observe the largest nonlinear enhancement ΔI_{DFG} for all E_F values.

In this measurement, the central pump wavelength is 1560 nm and the time delay is tunable from -5 ps to +5 ps. The soliton pulse width for the pump and probe combs are ≈ 430 fs and ≈ 110 fs respectively (Supplementary Section S3). The enhanced probe intensities are plotted in the bottom panels of Fig. 3b, 3c and 3d: all the ΔI_{DFG} peaks have a time-width of ≈ 500 fs in sech^2 fitting, as expected from a parametric process given the pulse duration of the pump and probe pulses used in our experiments. Such fast response of the GDF device is highly promising for high-speed devices and logic operations.

Finally, the co-existence of multiple electrically tunable plasmons allows us to perform logic operations, as schematically shown in Fig. 4a. Two parallel electrical signal generators (V_A and V_B the other contact is grounded) are used as input and each of them can provide either 0 V (OFF state, digital signal 0) or 0.5 V (ON state, digital signal 1). By combining the different states of V_A and V_B (*i.e.*, both ON, only one ON or both OFF), the graphene's E_F can be tuned to 0 eV, 0.24 eV and 0.4 eV. The pump and probe beams are launched into the GDF in opposite direction and we detect the gate-tunable plasmon generation via the DFG as an increase in the probe intensity (ΔI_{DFG}) at specific frequencies. For logic operations, three ΔI_{DFG} peaks (defined by the three plasmonic dispersion branches) with f_{sp} in the 0 ~ 50 THz band are filtered using three band-pass filters (BPF) based on fiber Bragg gratings (the spectral characterization of the filters is shown in Supplementary Section S3).

Figure 4b explains the filtering scheme more in details in the retrieved ' E_F - f_{sp} ' map. When increasing the $|E_F|$ from 0.1 eV to 0.4 eV, the f_{sp} of the three branches shifts in different ways. For instance, the low frequency branch shifts from 7.5 THz to 12.2 THz, while the middle and high frequency branches experience almost no shift (< 1.5 THz). On the other hand, as previously discussed (see Fig. 2), the middle frequency branch at 26 ~ 27 THz appears only for $|E_F| > 0.15$ eV, while the high frequency branch at ≈ 37 THz appears for $|E_F| > 0.25$ eV due to plasmon-phonon interaction. By selecting the filtering frequency to 7.5 THz, 27 THz and 37 THz with respect to the pump frequency, we can thus obtain the three different optical logic outputs. In particular, the ΔI_{DFG} from BPF3 is detectable only when both V_A and V_B are 'ON' (AND gate); the ΔI_{DFG} from BPF2 is detectable when either V_A or V_B is 'ON' (OR gate) while the ΔI_{DFG} from BPF1 is detectable only when both V_A and V_B are 'OFF' (NOR gate). Fig. 4c shows a measured example of the optical logic operations. We design two square-wave modulated signal traces for both V_A and V_B (0.5 V RZ code, sampling rate 1 MHz, data stream 100 kbps). Accordingly, the different BPFs provide at the output the logic operation expected from the AND, OR and NOR gates. Specifically, the signal-to-noise ratios of the AND, OR, and NOR gate outputs are higher than 89%, 82%, and 77% respectively, thus allowing a precise discrimination of the logic operation.

Conclusion

In conclusion, we used two synchronized counter-propagating laser combs to excite multiple electrically tunable plasmons *via* difference frequency generation and parametric amplification in a graphene/D-shaped fiber device and demonstrate their potential for integrated logic operations. By electrically tuning the graphene's Fermi level, the co-generated plasmons in the frequency range 7.5 THz to 37 THz can be

independently controlled and, after proper filtering, they can be used to realize three optoelectronic logic gates (AND, OR and NOR) in one-single device. The optical generation and electrical control of multiple graphene's plasmons provide a novel platform for nanoscale integrated optoelectronic devices with a high potential impact in advanced applications such as ultrafast light-field manipulating, signal processing and optoelectronic computing.

Methods

Theoretical analysis. The electrical field distribution inside the GDF was modeled using the finite element method. The graphene plasmonic dispersion and phonon coupling was calculated within the random phase approximation. The $\chi^{(2)}$ of graphene is estimated using the density matrix equations. More details are discussed in Supplementary Section S1.

Nanofabrication of the graphene heterostructure on a D-shaped fiber. The D-shaped fiber samples were prepared by side-polishing a commercial single mode silica fiber. The length of the D-shaped region is 2 mm and the insertion loss of the D-shaped fiber at 1560 nm is < 1 dB. Single layer graphene (SLG) was grown via CVD on Cu foil (99.8% pure) and then transferred onto the D-shaped fiber by using the polymethyl methacrylate (PMMA)-based wet transfer method. After bathing the PMMA/SLG/D-fiber in acetone and water, the PMMA was removed. Then 30nm/10nm Au/Ti electrodes were deposited via the masked sputtering method. The effective area of the on-fiber graphene interacting with light is 10 $\mu\text{m} \times$ 200 μm . Details are shown in Supplementary Section S2.

Optical frequency comb sources and experimental set-up. A stabilized mode locked fiber laser with central wavelength 1560 nm, fixed repetition 38 MHz, and pulse width \approx 300 fs is divided in two paths. The first one has 3dB spectral bandwidth \approx 6 nm and it is used as the pump, while the second one is supercontinuum-broadened to cover the spectral range 1560 nm \sim 2100 nm and it acts as the probe. To ensure the highest accuracy during measurement, the frequency combs are stabilized with total relative intensity noise < -120 dB and phase noise < -150 dBc/Hz at 10kHz. For the DFG plasmon detection we carefully implemented the following points: (1) both the pump and the probe are TM polarized, in order to maximize the graphene-light interaction and to probe its out-of-plane direction; (2) a tunable free-space delay line is used to precisely control the counter-launched pulses, with motion accuracy < 1 μm ; (3) the maximum peak power of the pump reaches 10 kW, much higher than the graphene saturable absorption threshold. The different logic gates (AND, OR and NOR) are selected via three different band pass filters based on fiber Bragg gratings with slightly tunable (\approx 10 nm) central wavelength for the optimization of the output intensity. Details of the experimental set-up are shown in Supplementary Section S3.

Declarations

Author contributions

B.Y. led this research and Y.R. led the team. Yuan L. and B.Y. led the device design and fabrication. Yiwei L., N.A. Y.W., B.C. and T.T. performed the experiments. Z.L. and Yuan L. contributed to the graphene heterostructure fabrication and to the electrical measurements. J.H. and Y.W. provided the D-shaped fiber samples and optimized the device. X.X. and J.H. contributed to the optical filtering. B.Y., X.G. and G.S. performed the physical analysis. All authors processed and analyzed the results. B.Y., Yiwei L., Yuan L., G.S., and Y.R. prepared the manuscript.

Acknowledgments. The authors acknowledge support from the National Science Foundation of China (61975025, U2130106), the Key project of Zhejiang Laboratory (2020KFY00562), and the National Key Research and Development Program (2021YFB2800602). This work was also supported by the European Union's Horizon 2020 research and innovation program under Grant Agreement GrapheneCore3 881603. G.S. acknowledges the German Research Foundation DFG (CRC 1375 NOA project B5) and the Daimler und Benz foundation for financial support.

Data availability. The data that support the plots within this paper and other findings of this study are available from the corresponding author on reasonable request. Source data are provided with this paper.

Competing interests. The authors declare no competing financial interests.

References

1. Caulfield, H. J. & Dolev, S. Why future supercomputing requires optics. *Nat. Photonics* **4**, 261–263 (2010).
2. Athale, R. & Psaltis, D. Optical Computing: Past and Future. *Opt. Photonics News* **27**, 32 (2016).
3. Xomalis, A. *et al.* Fibre-optic metadvice for all-optical signal modulation based on coherent absorption. *Nat. Commun.* **9**, 182 (2018).
4. Koos, C. *et al.* All-optical high-speed signal processing with silicon–organic hybrid slot waveguides. *Nat. Photonics* **3**, 216–219 (2009).
5. Klimmer, S. *et al.* All-optical polarization and amplitude modulation of second-harmonic generation in atomically thin semiconductors. *Nat. Photonics* **15**, 837–842 (2021).
6. Silva, A. *et al.* Performing Mathematical Operations with Metamaterials. *Science* **343**, 160–163 (2014).
7. Kwon, H., Sounas, D., Cordaro, A., Polman, A. & Alù, A. Nonlocal Metasurfaces for Optical Signal Processing. *Phys. Rev. Lett.* **121**, 173004 (2018).
8. Xu, X. *et al.* 11 TOPS photonic convolutional accelerator for optical neural networks. *Nature* **589**, 44–51 (2021).
9. Feldmann, J. *et al.* Parallel convolutional processing using an integrated photonic tensor core. *Nature* **589**, 52–58 (2021).
10. Won, R. Intelligent learning with light. *Nat. Photonics* **12**, 571–573 (2018).

11. Lin, X. *et al.* All-optical machine learning using diffractive deep neural networks. *Science* **361**, 1004–1008 (2018).
12. Tan, T. *et al.* Predicting Kerr Soliton Combs in Microresonators via Deep Neural Networks. *J. Light. Technol.* **38**, 6591–6599 (2020).
13. Genty, G. *et al.* Machine learning and applications in ultrafast photonics. *Nat. Photonics* **15**, 91–101 (2021).
14. Kok, P. *et al.* Linear optical quantum computing with photonic qubits. *Rev. Mod. Phys.* **79**, 135–174 (2007).
15. Miller, D. A. B. Are optical transistors the logical next step? *Nat. Photonics* **4**, 3–5 (2010).
16. Fushimi, A. & Tanabe, T. All-optical logic gate operating with single wavelength. *Opt. Express* **22**, 4466 (2014).
17. Xu, Q. & Lipson, M. All-optical logic based on silicon micro-ring resonators. *Opt. Express* **15**, 924 (2007).
18. Sun, C. *et al.* Single-chip microprocessor that communicates directly using light. *Nature* **528**, 534–538 (2015).
19. Ota, M., Sumimura, A., Fukuhara, M., Ishii, Y. & Fukuda, M. Plasmonic-multimode-interference-based logic circuit with simple phase adjustment. *Sci. Rep.* **6**, 24546 (2016).
20. Ying, Z. *et al.* Electronic-photonic arithmetic logic unit for high-speed computing. *Nat. Commun.* **11**, 2154 (2020).
21. Zheludev, N. I. What diffraction limit? *Nat. Mater.* **7**, 420–422 (2008).
22. Alcaraz Iranzo, D. *et al.* Probing the ultimate plasmon confinement limits with a van der Waals heterostructure. *Science* **360**, 291–295 (2018).
23. Koppens, F. H. L., Chang, D. E. & García de Abajo, F. J. Graphene Plasmonics: A Platform for Strong Light–Matter Interactions. *Nano Lett.* **11**, 3370–3377 (2011).
24. Gramotnev, D. K. & Bozhevolnyi, S. I. Plasmonics beyond the diffraction limit. *Nat. Photonics* **4**, 83–91 (2010).
25. Grigorenko, A. N., Polini, M. & Novoselov, K. S. Graphene plasmonics. *Nat. Photonics* **6**, 749–758 (2012).
26. Chen, J. *et al.* Optical nano-imaging of gate-tunable graphene plasmons. *Nature* **487**, 77–81 (2012).
27. Fei, Z. *et al.* Gate-tuning of graphene plasmons revealed by infrared nano-imaging. *Nature* **487**, 82–85 (2012).
28. Tan, T., Jiang, X., Wang, C., Yao, B. & Zhang, H. 2D Material Optoelectronics for Information Functional Device Applications: Status and Challenges. *Adv. Sci.* **7**, 2000058 (2020).
29. Constant, T. J., Horneett, S. M., Chang, D. E. & Hendry, E. All-optical generation of surface plasmons in graphene. *Nat. Phys.* **12**, 124–127 (2016).
30. Yao, X., Tokman, M. & Belyanin, A. Efficient Nonlinear Generation of THz Plasmons in Graphene and Topological Insulators. *Phys. Rev. Lett.* **112**, 055501 (2014).

31. Basov, D. N., Fogler, M. M. & Garcia de Abajo, F. J. Polaritons in van der Waals materials. *Science* **354**, aag1992–aag1992 (2016).
32. Tan, T. *et al.* Multispecies and individual gas molecule detection using Stokes solitons in a graphene over-modal microresonator. *Nat. Commun.* **12**, 6716 (2021).
33. Yao, B. *et al.* Broadband gate-tunable terahertz plasmons in graphene heterostructures. *Nat. Photonics* **12**, 22–28 (2018).
34. Nikitin, A. Y. Telecom meets terahertz. *Nat. Photonics* **12**, 3–4 (2018).
35. Diddams, S. A. The evolving optical frequency comb [Invited]. **27**, (2010).
36. Qin, C. *et al.* Electrically controllable laser frequency combs in graphene-fibre microresonators. *Light Sci. Appl.* **9**, 185 (2020).
37. Schwierz, F. Graphene transistors. *Nat. Nanotechnol.* **5**, 487–496 (2010).
38. An, N. *et al.* Electrically Tunable Four-Wave-Mixing in Graphene Heterogeneous Fiber for Individual Gas Molecule Detection. *Nano Lett.* **20**, 6473–6480 (2020).
39. Soavi, G. *et al.* Broadband, electrically tunable third-harmonic generation in graphene. *Nat. Nanotechnol.* **13**, 583–588 (2018).
40. Soavi, G. *et al.* Hot Electrons Modulation of Third-Harmonic Generation in Graphene. *ACS Photonics* **6**, 2841–2849 (2019).
41. Yao, B. *et al.* Gate-tunable frequency combs in graphene–nitride microresonators. *Nature* **558**, 410–414 (2018).
42. Meric, I. *et al.* Current saturation in zero-bandgap, top-gated graphene field-effect transistors. *Nat. Nanotechnol.* **3**, 654–659 (2008).
43. Cerullo, G. & De Silvestri, S. Ultrafast optical parametric amplifiers. *Rev. Sci. Instrum.* **74**, 1–18 (2003).
44. Hwang, E. H., Sensarma, R. & Das Sarma, S. Plasmon-phonon coupling in graphene. *Phys. Rev. B* **82**, 195406 (2010).
45. Yan, H. *et al.* Damping pathways of mid-infrared plasmons in graphene nanostructures. *Nat. Photonics* **7**, 394–399 (2013).
46. Marini, A., Cox, J. D. & García De Abajo, F. J. Theory of graphene saturable absorption. *Phys. Rev. B* **95**, 1–11 (2017).

Figures

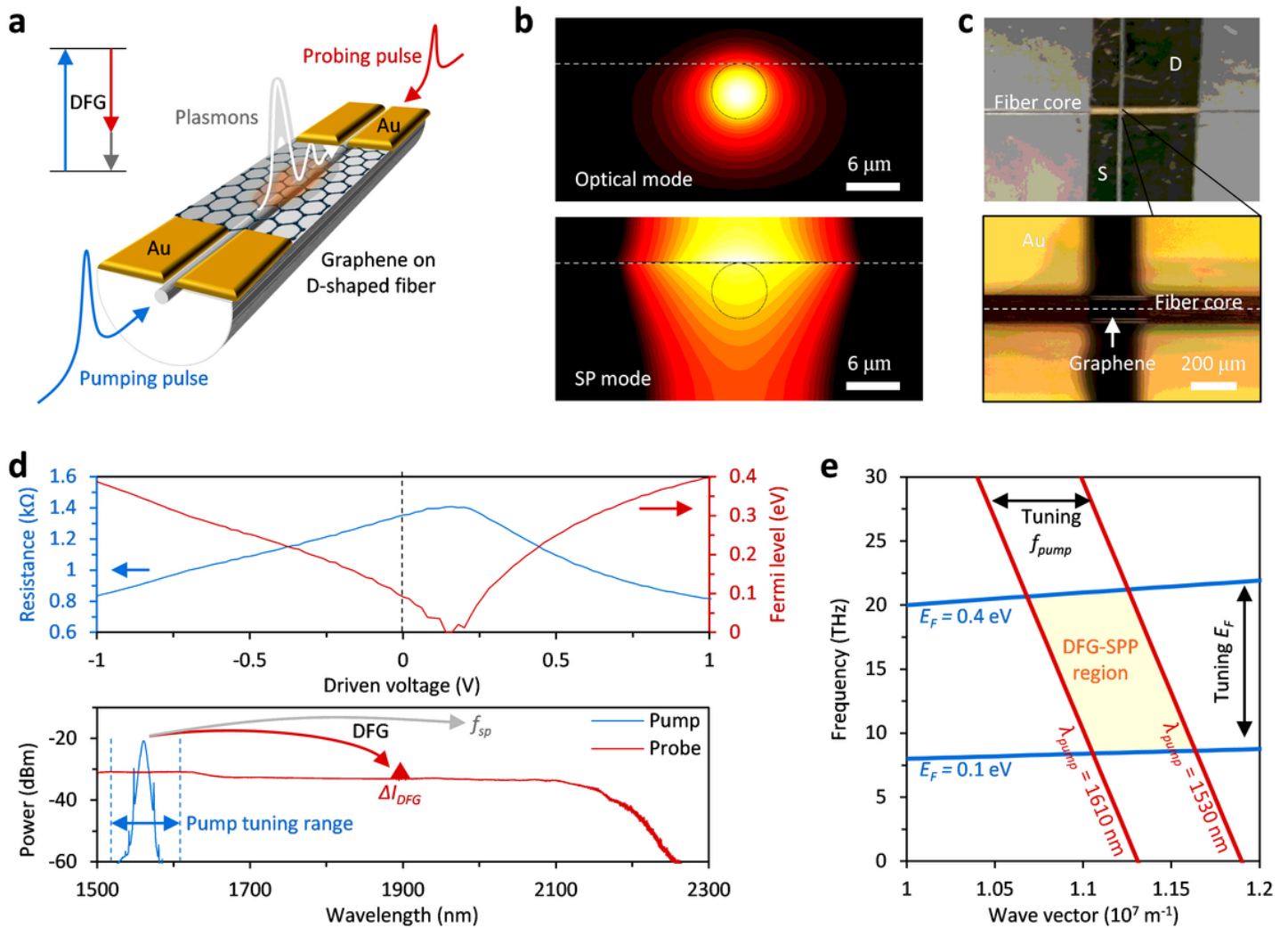


Figure 1

Generation and control of graphene's plasmons in a graphene heterogeneous fiber device. **a**, Schematic of the graphene optoelectronic device deposited on a D-shaped fiber. DFG via the surface $\chi^{(2)}$ nonlinearity is excited by two counter-propagating synchronized pulses. Inset: energy conservation for the DFG process. **b**, Simulated electrical field distributions of an optical mode propagating in the fiber core and a plasmonic mode propagating along the graphene-fiber interface (transverse magnetic polarization). SP mode: surface-plasmon mode **c**, Top-view microscope image of the graphene transistor on-fiber. The white dashed line shows the fiber core, the monolayer graphene is connected by two Au electrodes, with contact channel length 200 μm . **d**, Top panel: Measured resistance and calculated Fermi level, the sampling rate is 20 mV. Bottom panel: Spectra of the pump comb (blue) and the probe comb (red). The red and grey arrows illustrate the DFG process. **e**, Parametric space of the DFG plasmons. The blue curves show the electrically tunable dispersion of graphene, while the red curves show the optically tunable phase-matching condition.

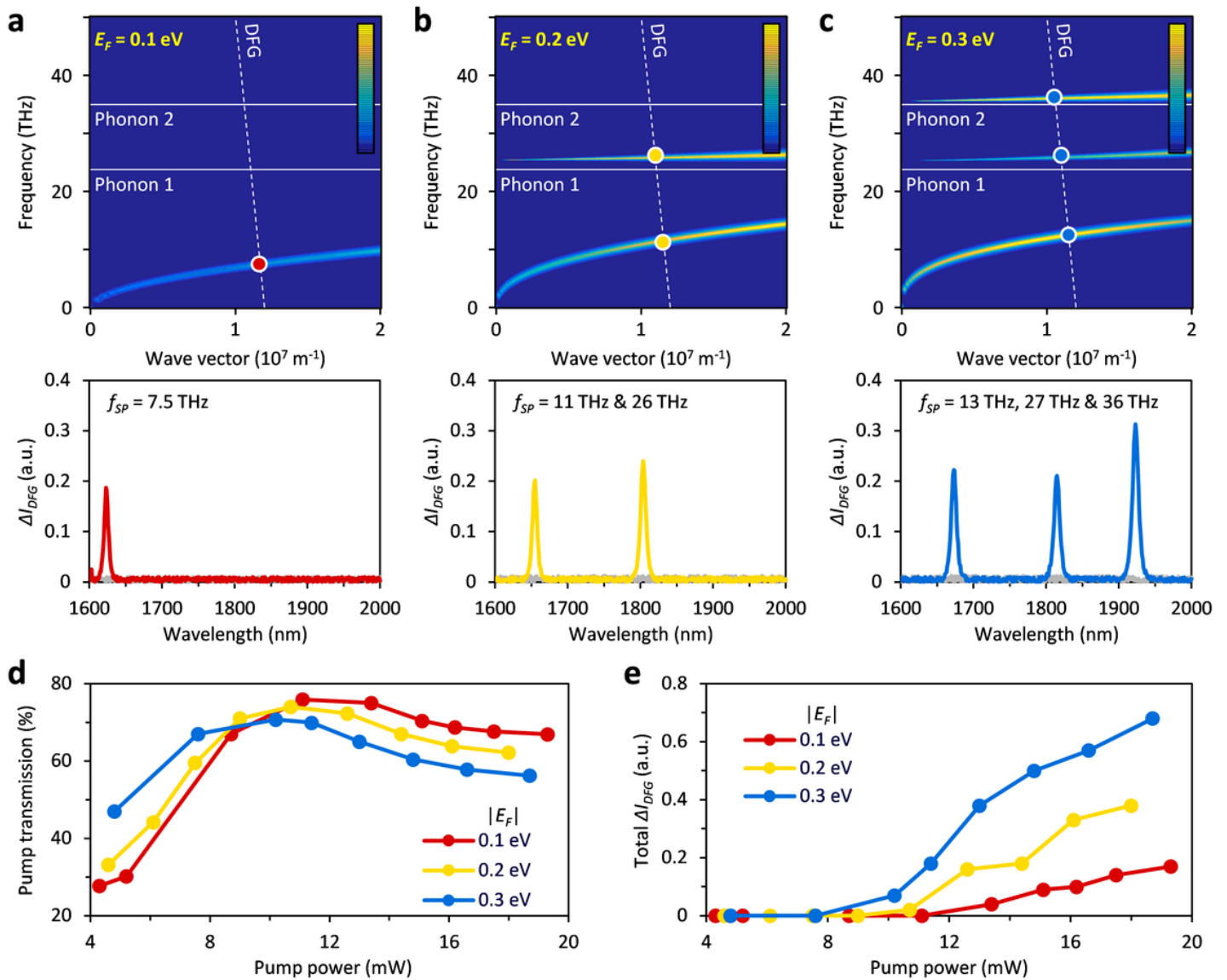


Figure 2

DFG signal and electrically tunable plasmons. **a to c**, Top panels: Phase-matching condition (white dashed line) and graphene's plasmonic dispersion for $|E_F| = 0.1, 0.2$ and 0.3 eV. The red, yellow and blue dots mark the 'frequency-momentum' position of the nonlinearly generated plasmons. Bottom panels: measured ΔI_{DFG} peaks. Red, yellow and blue curves plot the cases when $|E_F| = 0.1, 0.2$ and 0.3 eV, respectively. In these panels, the grey curves show the results measured in a D-shaped fiber without graphene for comparison. Color bar of the maps shows normalized plasmonic intensity. **d**, Pump transmission in the GDF device. The pump transmission first increases due to saturable absorption, and then decreases due to nonlinear DFG consumption. **e**, The total ΔI_{DFG} increases linearly with the pump power.

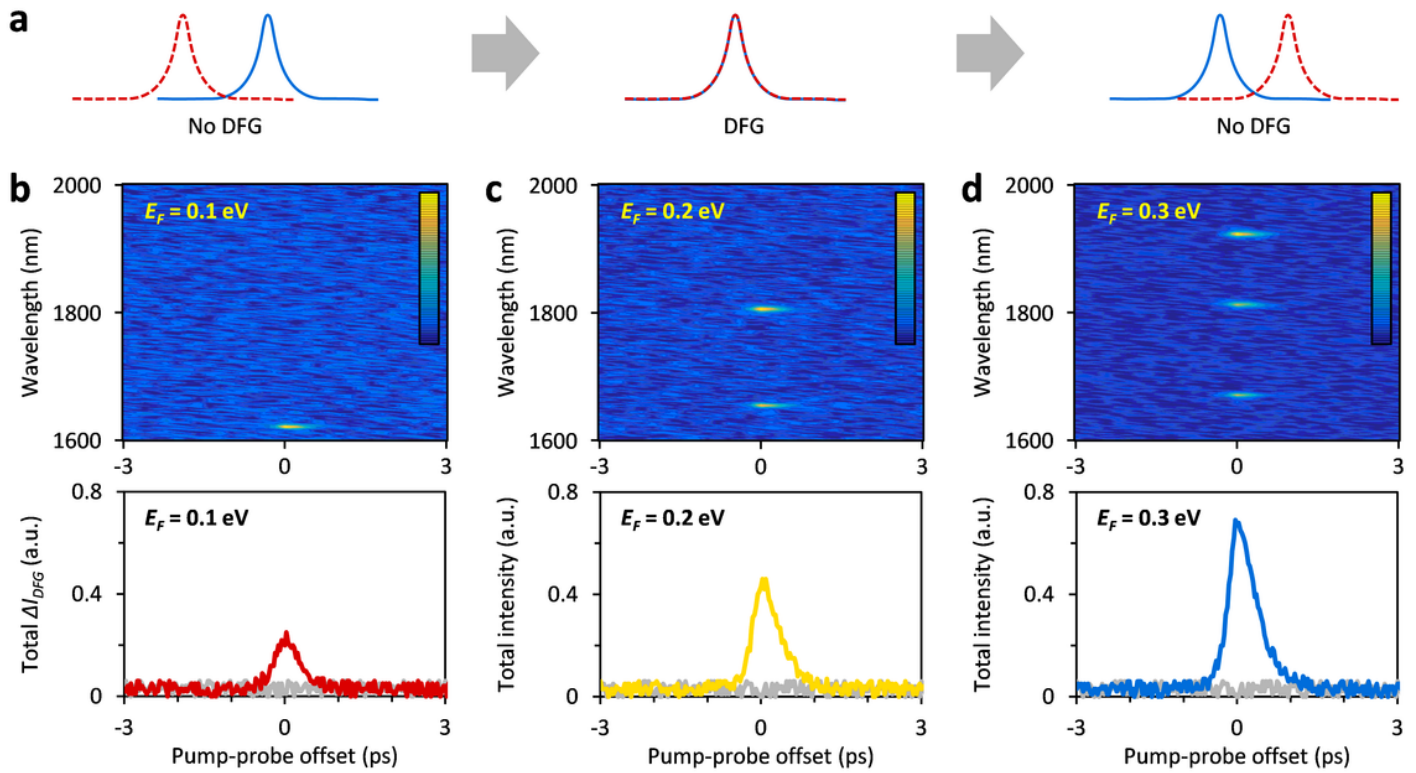


Figure 3

Time-correlation measurements of the plasmon generation *via* DFG. **a**, Sketch of the time-correlation experiment, DFG occurs only when the pump and the probe overlap in time. **b** to **d**, The top panels show the ΔI_{DFG} maps corresponding to different f_{sp} , when the graphene's Fermi level is 0.1, 0.2 and 0.3 eV; the bottom panels plot the total (integrated) ΔI_{DFG} traces in the three cases. The grey curves show the reference signal (background) when $f_{pump} - f_{probe}$ is far from the plasmonic resonances.

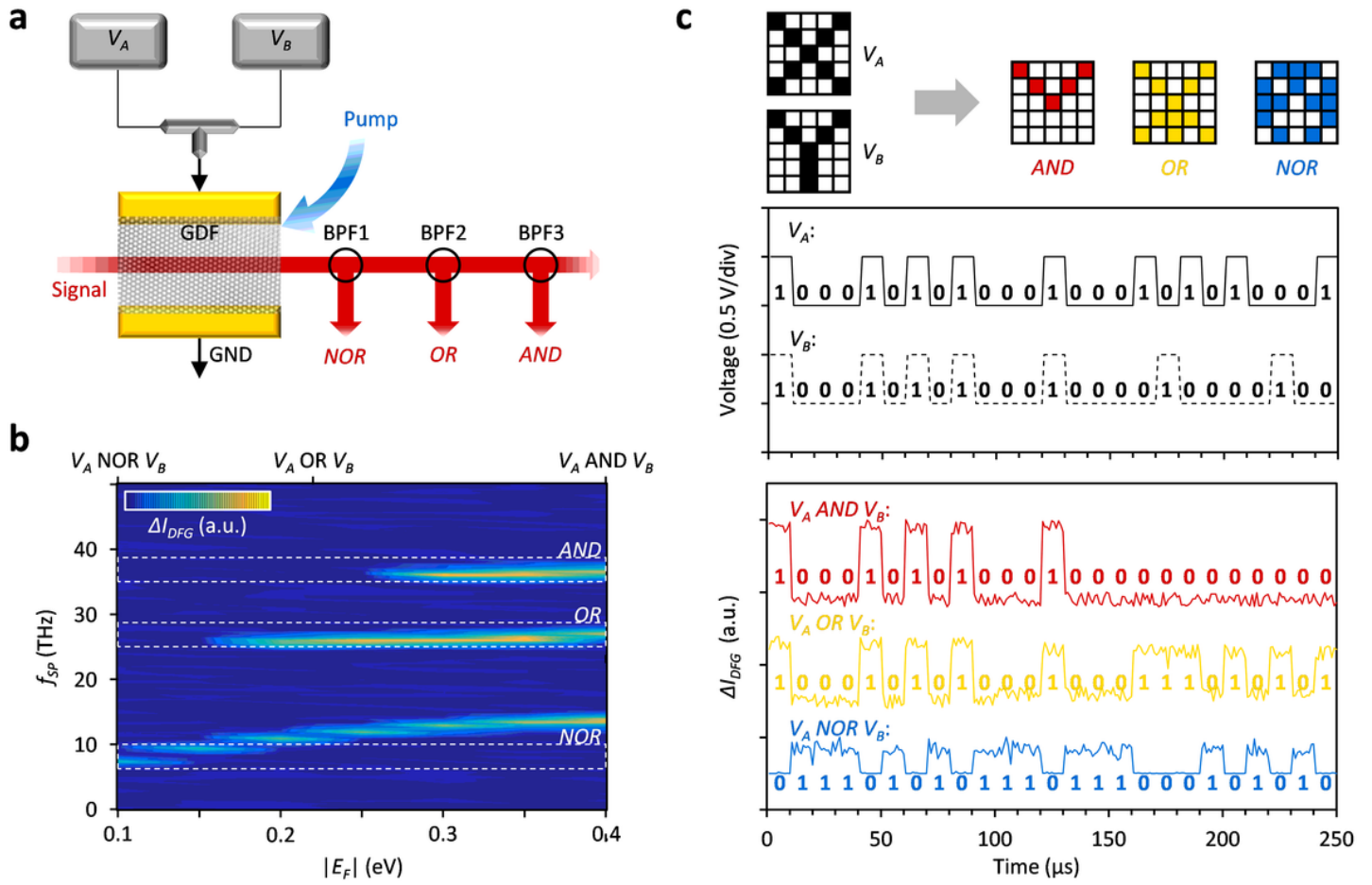


Figure 4

Electrooptic logic operations and gates. **a** Schematic design of the setup to obtain the logic outputs NOR, OR and AND using three band-pass filters (BPFs). Here V_A and V_B are two independent digital signals used to tune the graphene $|E_F|$. **b**, Results of the filtering in the $|E_F|$ - f_{SP} space for the frequencies 7.5 THz, 27 THz and 36 THz selected by the three BPFs and corresponding to the three logic operation of NOR, OR, AND. **c**, Example of logic operations measured at the outputs of the three BPFs, here the black curves plot the amplitudes of V_A and V_B while red, yellow and blue curves show the output of the AND, OR, NOR gates.

Supplementary Files

This is a list of supplementary files associated with this preprint. Click to download.

- [003SIGS2.docx](#)